This article has been accepted for publication in IEEE Transactions on Instrumentation and Measurement. This is the author's version which has not been fully edited and content may change prior to final publication. Citation information: DOI 10.1109/TIM.2025.3545170

Design of eddy current testing probe for thickness evaluation of multilayers on nuclear fuel claddings

Jiuhao Ge(葛玖浩), Fei Xu(徐飞), Jia Chen(陈嘉), Weiyu Jiang(蒋维宇), and Zhiyong Deng(邓志勇)

***Abstract*—Nuclear fuel claddings are the first barrier against fission products in a primary circuit. Eddy current testing is a commonly used nondestructive testing technique for measuring the thickness of chromium and oxide layers on claddings. Due to lack of the analytical model for eddy current testing probes above multilayer pipes, the design and optimization of the probe has not been reported. In this paper, an analytical model for coils placed outside multilayer pipes involving arbitrary nonconductive and conductive layers was built based on second-older vector potential. A model of nuclear fuel claddings was built, and the influence of probe parameters on signals was analyzed. According to the results, a design flowchart for the eddy current testing probe is provided by considering resonance frequency and quality factor. Comparisons among the experiment, finite element model, and analytical model indicate that the built analytical model is validated and efficient. In addition, the performance of the new probe is better and more sensitive than that of the old probe. Therefore, the proposed design flowchart is effective.**

***Index Terms*—analytical model, pancake coil, chromium layer, oxide layer**

I. Introduction

The nuclear fuel utilized in reactors is comprised of fuel rods, which are long pipes made from zirconium (Zr) alloys [1]. These pipes are filled with uranium dioxide pellets, and the pipes are commonly referred to as nuclear fuel cladding. These nuclear fuel claddings are typically coated with a chromium (Cr) layer on the outside. This Cr layer can generate a dense Cr_2O_3 layer with water at 1273 K or higher, which drastically reduces the diffusion of oxygen [2]. The Cr_2O_3 layer, Cr layer, and Zr pipe consist of multilayer pipes that act as the first barrier against fission products in the primary circuit. Thus, it is crucial to measure the thickness of multilayers to ensure the safety and integrity of fuel rods during service [3].

Eddy current testing (ECT) is a commonly used nondestructive testing technique for measuring nuclear fuel claddings. It uses the difference between the primary magnetic field and the secondary magnetic field or the impedance change resulting from the interaction between the eddy current and the conductor specimen to detect defects and measure the thickness of materials [4, 5]. Using a pancake probe, ECT enables the precise inspection of chalk river unidentified deposits, oxide, and coating thickness in nuclear fuel claddings [6, 7]. Moreover, many studies have investigated the thickness evaluations of fuel claddings [8–10].

Optimal ECT probe design effectively improves the performance and probability of detection of the ECT technique [11–15]. Several studies have reported on the design of ECT probes for plate detection [16–18]. In these studies, finite element simulation was used to analyze the influence of probe parameters on signals, assisting in the design of probes [19–23]. However, in the case of thickness measurements of the oxide layer (nonconductive, <100 μm) and the Cr layer (conductive, <25 μm) on fuel claddings, scant research has reported on relevant finite element analyses or further design. The main challenge here lies in the significant size disparities among the oxide layer, Cr layer, Zr pipe (with a thickness of about 8 mm), and probes (around 3 mm in diameter). Achieving convergence in finite element method (FEM) requires a substantial number of elements, which in turn greatly increases computation time and computational load.

The analytical model is another simulation method for ECT problems that does not consider element mesh [24–26]. Compared to the finite element method, the analytical model has the advantage of simplicity, higher speed, and lower computational resource load. It is widely used in symmetrical ECT problems [27, 28]. Second-older vector potential (SOVP) has been proposed to solve asymmetrical ECT problems, involving pancake probes placed above conductive cylinders [29, 30]. Using SOVP, an asymmetrical model of a pancake probe placed above a pipe was built [31]. Compared to the method in [30], the work proposed a straightforward method for

This work was funded by the National Key R&D Program of China (No. 2022YFC3005003) and the National Natural Science Foundation of China (No. 61903191).

Jiuhao Ge, Fei Xu, and Jia Chen are with Nondestructive Detection and Monitoring Technology for High Speed Transportation Facilities, Key Laboratory of Ministry of Industry and Information Technology, Nanjing University of Aeronautics and Astronautics, Nanjing, Jiangsu, 211106, China, (The corresponding author is Jiuhao Ge: gejiuhao@nuaa.edu.cn).

Weiyu Jiang and Zhiyong Deng are with Nuclear Power Institute of China, Chengdu, Sichuan, China.

This article has been accepted for publication in IEEE Transactions on Instrumentation and Measurement. This is the author's version which has not been fully edited and content may change prior to final publication. Citation information: DOI 10.1109/TIM.2025.3545170

calculating the coil coefficient in the cylindrical coordinate system. The work simplified the solving process of the solution for coils placed near a conductive pipe. Based on SOVP, [33, 34] provided analytical solutions for flexible circular coils inside a pipe and outside a double-layer pipe with an air gap.

According to the above literature review, research on modeling coils placed outside a single pipe or double-layer pipe with gap has been proposed. However, the development of a model for coils outside multilayer pipes with arbitrary nonconductive and conductive layers remains unexplored. This limitation hindered the simulation of multilayer pipes and the optimization of probe designs for nuclear fuel claddings.

Thus, based on the background of designing an ECT pancake probe for thickness evaluation of multilayers on fuel claddings. First, expanding the method developed in [31], an analytical model of a coil above a multilayer pipe fitting for any nonconductive and conductive layers is built in Section II. The influence of exciting frequency and coil geometrical parameters on the sensitivity of the probe is analyzed through the analytical model. The designing guidance of the probe is summarized in Section III. A design flowchart of the probe is created in Section IV. Finally, in Section V, the built analytical model is validated and compared with the finite element method. Moreover, the performance of the old and new probes is compared through the experimental method.

II. Analytical Model of an Eddy Current Testing Probe above multilayers on pipe

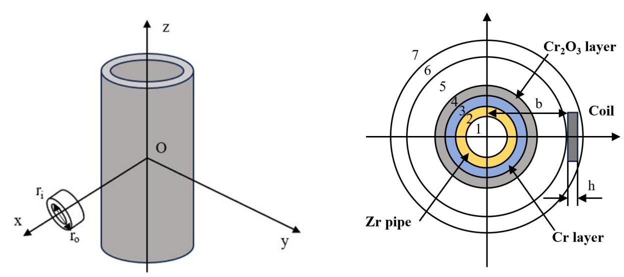

Fig. 1. Illustration of a model for a coil placed above a multilayer rod.

The analytical model for the measurement of multilayer pipe using ECT is illustrated in Fig. 1. Nuclear fuel cladding was used as an example for a case with two conductive layers and one nonconductive layer. More complex cases can also be solved using the proposed model. There are three regions in actual claddings: the Zr pipe, Cr layer, and Cr_2O_3 layer. Then, the model is divided into seven sub-regions: region 1 is air, $\rho<r_1$; region 2 is the Zr pipe, $r_1<\rho<r_2$; region 3 is the Cr layer, $r_2<\rho<r_2+d_1$; region 4 is the oxide layer, $r_2+d_1<\rho<r_2+d_1+d_2$; region 5 is air, $r_2+d_1+d_2<\rho<b$; region 6 is air containing coils, $b<\rho<\sqrt{(b+h)^2+r_o}$; and region 7 is air, $\rho>\sqrt{(b+h)^2+r_o}$. The inner radius of the Zr pipe is r_1, while the outer radius is r_2. The conductivity of the Zr pipe is σ_1, and the relative permeability is μ_{r1}. The conductivity of the Cr layer is σ_2, and the relative permeability is μ_{r2}. The thickness of the Cr layer is d_1. The oxide layer is nonconductive, and its thickness is denoted as d_2. The parameters of the coil are inner radius r_i, outer radius r_o, height h, and turns N.

To solve the asymmetrical eddy current problem, second-order magnetic vector potential is used to describe the asymmetrical eddy current field. Either one or two scalar equations are needed to analytically describe the three-dimensional electromagnetic field. The relationship between magnetic vector potential $\boldsymbol{A}$ and the second-order magnetic vector potential $\boldsymbol{W}$ is shown in (1). This greatly simplifies the three-dimensional eddy current field problem.

$$\boldsymbol{A} = \nabla \times \boldsymbol{W} \tag{1}$$

In the cylindrical coordinate system, $\boldsymbol{W}$ can be expressed as:

$$\boldsymbol{W} = W_a \boldsymbol{e_z} + \boldsymbol{e_z} \times \nabla W_b, \tag{2}$$

where W_a and W_b are second-order potentials that satisfy the following scalar Helmholtz equation:

$$\begin{aligned} \nabla^2 W_a + k^2 W_a = 0 \\ \nabla^2 W_b + k^2 W_b = 0, \end{aligned} \tag{3}$$

where $k^2 = -i\omega\sigma\mu_0$, magnetic flux density $\boldsymbol{B}$ can be expressed as:

$$\boldsymbol{B} = \nabla\left(\frac{\partial W_a}{\partial z}\right) + k^2 (W_a \boldsymbol{e_z} + \boldsymbol{e_z} \times \nabla W_b). \tag{4}$$

Since the conductivity of the air region and the oxide layer region is 0, the magnetic flux density in regions 1, 4, and 5 is only related to W_a. W_a should satisfy the scalar Laplace equation:

$$\nabla^2 W_a = 0. \tag{5}$$

Magnetic flux density in regions 1, 4, and 5 is

$$\boldsymbol{B} = \nabla\left(\frac{\partial W_a}{\partial z}\right). \tag{6}$$

Given the separating variable method and the physical restrictions that W_a is finite for $\rho \to 0$, the expressions of potentials in regions 1, 2, 3, and 4 are provided as follows:

$$W_{a1} = \int_{-\infty}^{\infty} \sum_{m=-\infty}^{\infty} C_1 \, \mathrm{I}_m(|\alpha|\rho) e^{im\phi} e^{i\alpha z} d\alpha \tag{7}$$

$$W_{a2} = \int_{-\infty}^{\infty} \sum_{m=-\infty}^{\infty} [C_{a2} \, \mathrm{I}_m(\alpha_{k1}\rho) + D_{a2} \mathrm{K}_m(\alpha_{k1}\rho)] e^{im\phi} e^{i\alpha z} d\alpha \tag{8}$$

$$W_{b2} = \int_{-\infty}^{\infty} \sum_{m=-\infty}^{\infty} [C_{b2} \, \mathrm{I}_m(\alpha_{k1}\rho) + D_{b2} \mathrm{K}_m(\alpha_{k1}\rho)] e^{im\phi} e^{i\alpha z} d\alpha \tag{9}$$

$$W_{a3} = \int_{-\infty}^{\infty} \sum_{m=-\infty}^{\infty} [C_{a3} \, \mathrm{I}_m(\alpha_{k2}\rho) + D_{a3} \mathrm{K}_m(\alpha_{k2}\rho)] e^{im\phi} e^{i\alpha z} d\alpha \tag{10}$$

$$W_{b3} = \int_{-\infty}^{\infty} \sum_{m=-\infty}^{\infty} [C_{b3} \, \mathrm{I}_m(\alpha_{k2}\rho) + D_{b3} \mathrm{K}_m(\alpha_{k2}\rho)] e^{im\phi} e^{i\alpha z} d\alpha \tag{11}$$

$$W_{a4} = \int_{-\infty}^{\infty} \sum_{m=-\infty}^{\infty} [C_s \, \mathrm{I}_m(|\alpha|\rho) + D_{ec} \mathrm{K}_m(|\alpha|\rho)] e^{im\phi} e^{i\alpha z} d\alpha, \tag{12}$$

where $\alpha_{ki} = \sqrt{\alpha^2 - k_i^2}$, $k_i^2 = -j\omega\sigma_i\mu_0$, i=1, 2; I_m and K_m are modified Bessel functions of the first and second kinds of order m, respectively; C_1, C_{a2}, D_{a2}, C_{b2}, D_{b2}, C_{a3}, D_{a3}, C_{b3}, D_{b3} and D_{ec} are unknown coefficients; and C_s is the coil coefficient, which is related only to the geometry of the coil. The expression of C_s can be obtained by referring to [31] as follows:

$$C_s = n_c \int_b^{h+b} \mathrm{d}d \int_{r_i}^{r_o} C_{ss} \, \mathrm{d}r \tag{13}$$

where

This article has been accepted for publication in IEEE Transactions on Instrumentation and Measurement. This is the author's version which has not been fully edited and content may change prior to final publication. Citation information: DOI 10.1109/TIM.2025.3545170

$$C_{ss} = \frac{iu_0 I}{\alpha^2 \pi^2} \int_0^r (C_{s1} + C_{s2}) \sin\left(\alpha\sqrt{r^2 - \tau^2}\right) d\tau$$

$$C_{s1} = \frac{d|\alpha|}{\sqrt{d^2 + \tau^2}} K'_m(|\alpha|\sqrt{d^2 + \tau^2}) \cos\left(m * arctan\frac{\tau}{d}\right)$$

$$C_{s2} = \frac{m\tau}{d^2 + \tau^2} K_m(|\alpha|\sqrt{d^2 + \tau^2}) \sin\left(m * arctan\frac{\tau}{d}\right)$$

$$n_c = \frac{N}{(r_o - r_i)h}$$

Equations (7) to (12) can be solved by utilizing the boundary conditions on four surfaces. In single or double layers with gap cases, two kinds of boundary conditions were applied: the radial component continuity of the magnetic flux density on the surfaces of the conductive region and the tangential component continuity of the magnetic field on the surfaces of the conductive region. However, these nine functions cannot solve 10 unknown coefficients. To solve the multilayer pipe model containing arbitrary nonconductive and conductive layers, the radial component continuity of magnetic vector potential on the surface between the conductive regions was added.

Thus, using the proposed analytical model, the problem involving multilayer pipes with arbitrary nonconductive and conductive layers can be solved. A detailed example involving two adjacent conductive layers and one nonconductive layer above is shown in the Appendix. After obtaining C_s and D_{ec}, the impedance change of a coil placed near the pipe is expressed as follows:

$$\Delta Z = -\frac{i\omega 4\pi}{\mu_0 I^2} \int_{-\infty}^{\infty} \sum_{m=-\infty}^{\infty} \alpha^2 C_s(\alpha, m) D_{ec}(-\alpha, -m) d\alpha. \quad (14)$$

Combining C_s and D_{ec} with respect to the parity of α and m, the above equations can be simplified to

$$\Delta Z = \frac{i\omega 8\pi^2}{\mu_0 I^2} \int_0^{\infty} \sum_{m=-\infty}^{\infty} \alpha^2 C_s(\alpha, m) D_{ec}(\alpha, m) d\alpha. \quad (15)$$

III. Influence of Exciting Frequency and Coil Parameters on the Sensitivity of the ECT Probe

In this section, the influence of the exciting frequency and the coil parameters on the sensitivity of the ECT probe was analyzed using the model developed in Section II. The purpose of this section is to provide intuitive directions for improving the performance of the ECT probe from a design perspective.

A. Simulation Parameters

The parameters of the Zr tube in the simulation are shown in Table I. In addition, the parameters of the original coil in the probe provided by a commercial company are shown in Table II. The conductivity was measured by an AT510 resistance tester (Applent Instruments Inc. Changzhou, China), and permeability was measured by a BKT-4500 vibrating sample magnetometer (Shincotest Technology, Beijing, China).

TABLE I
Parameters of the Multilayer Zr Tube

Parameter	Zr tube	Cr layer	Oxide layer
Inner diameter (mm)	8.36	9.50	9.525
Thickness (μm)	570	0~200	0~100
Conductivity (S/m)	2.5×10E6	7.7×10E6	0.0
Relative permeability	1.0	1.0	1.0

TABLE II
Parameters of the Original Coil

Parameter	Value
Inner diameter (mm)	3
Outer diameter (mm)	4
Thickness (mm)	0.5
Height (mm)	7
Wire diameter (mm)	0.18
Turn	120
Bottom thickness of shell (mm)	1

To simplify the design of the coil, three parameters were considered. They are the mean diameter D_0, coil width w, and coil height H. Increasing the coil turn can dramatically improve the sensitivity of the coil. However, in our simulation, the coil turn or the coil section was fixed, and the combination of $w \times H$ was studied. In other words, whether tall or fat coils were better was studied. The exciting frequency f is a key parameter that determines the detectable thickness in the ECT. Thus, the relationship between the exciting frequency and the detectable thickness of the multilayer was studied. The detailed values of the coil parameters set in the simulation are shown in Table III.

TABLE III
Values of Coil Parameters in Simulation

Parameter	Values
f (Hz)	300k, 500k, 1M, 5M, 10M, 50M
D_0 (mm)	2.5, 3.0, 3.5, 4.0
w×H (mm)	0.5×7.0, 0.6×5.8, 0.7×5.0, 0.8×4.38, 0.9×3.89, 1.0×3.50

B. Influence of the Exciting Frequency

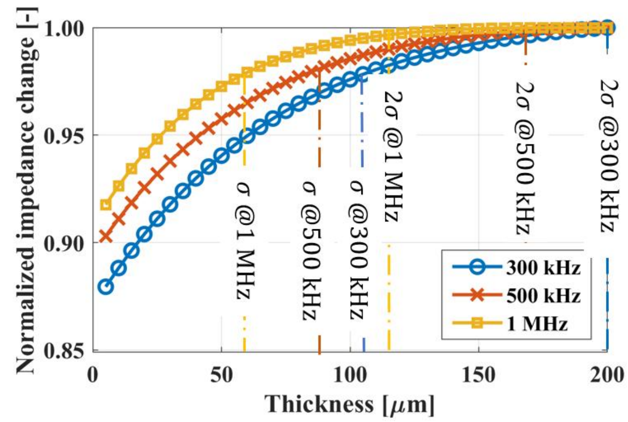

(a) 300 kHz, 500 kHz, and 1 MHz

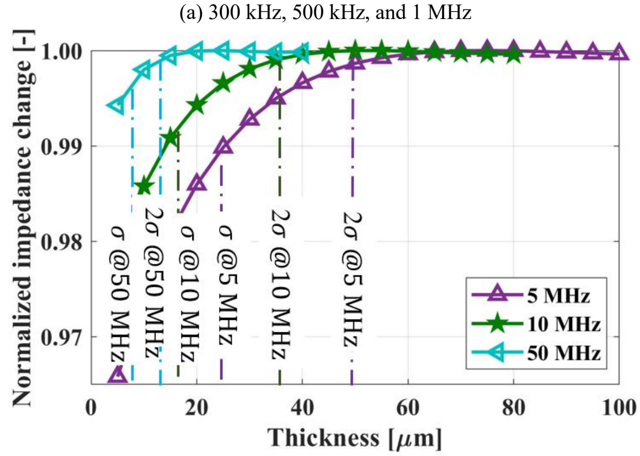

(b) 5 MHz, 10 MHz, and 50 MHz

Fig. 2. Influence of frequency on the impedance of the ECT signal of the Cr layer.

This article has been accepted for publication in IEEE Transactions on Instrumentation and Measurement. This is the author's version which has not been fully edited and content may change prior to final publication. Citation information: DOI 10.1109/TIM.2025.3545170

The influence of the exciting frequency on the ECT signals of the Cr layer is shown in Figs. 2 and 3. To compare the curve more clearly, the normalized amplitude change of the signals in Fig. 3 was mapped between 0 and 1. As shown in Figs. 2 and 3, with increasing Cr layer thickness, the amplitude and phase of the impedance change increases. With increasing frequency, the changes in signal amplitude and phase are increased, which means the sensitivity of the probe is also heightened. In addition, the linearity of the phase was higher than that of the amplitude. In this paper, the maximum detectable thickness is defined as the thickness after which the signal does not change with the thickness. Figs. 2 and 3 show that with increasing frequency, maximum detectable thickness decreases. The skin depths σ and 2σ of each frequency in the Cr layer are identified in the figures. Figures indicate that 2σ can approximately indicate the maximum detectable thickness.

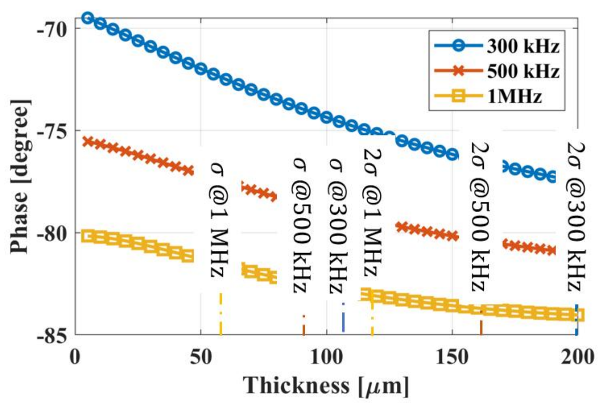

(a) 300 kHz, 500 kHz, and 1MHz

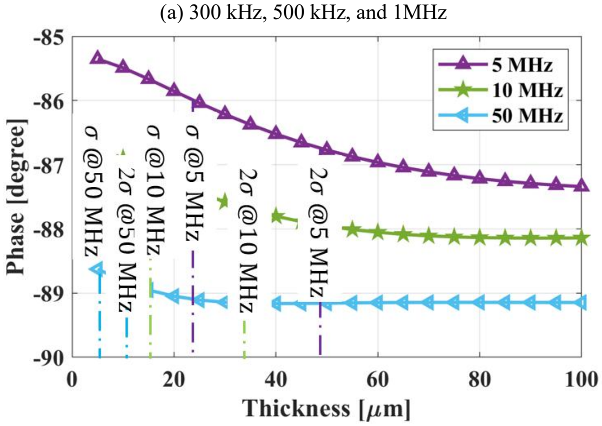

(b) 5 MHz, 10 MHz, and 50 MHz

Fig. 3. Influence of frequency on the phase of the ECT signal of the Cr layer.

The influence of the exciting frequency on the ECT signals of the oxide layer is shown in Fig. 4. With increasing oxide thickness, the amplitude of the impedance change decreases linearly, and the phase remains unchanged. With increasing frequency, the changes of amplitude and phase are increased. This means that with increasing frequency, the sensitivity of the probe increases.

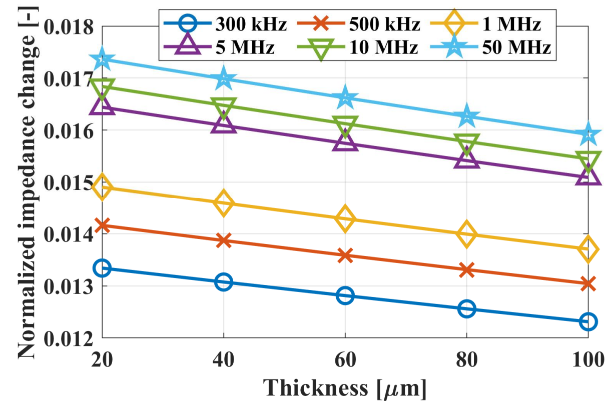

(a) Amplitude

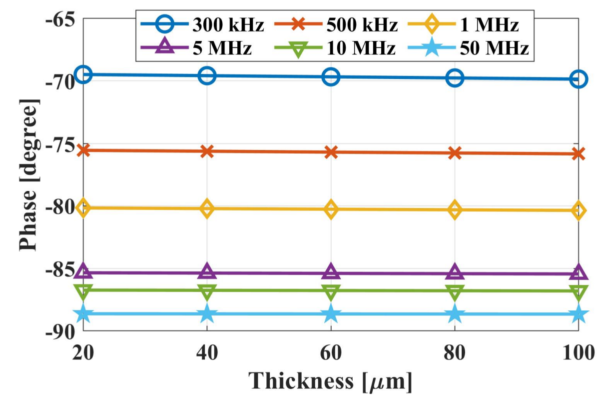

(b) Phase

Fig. 4. Influence of frequency on the ECT signal of the oxide layer.

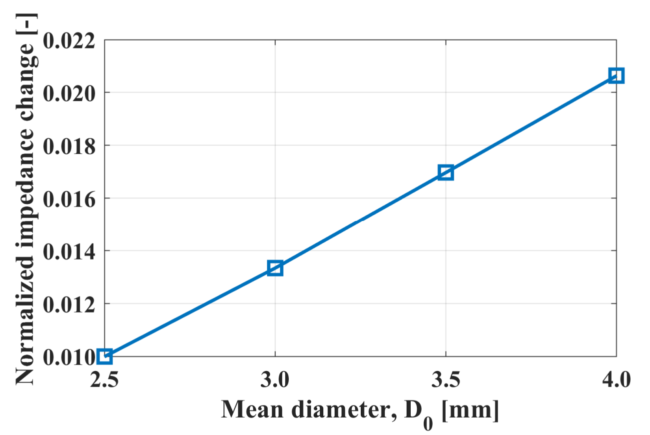

Fig. 5. Influence of coil mean diameter on ECT signal (f = 300 kHz, w(H) = 0.5 (7.0) mm, Cr layer = 5 μm, oxide layer = 20 μm).

C. Influence of Coil Mean Diameter

The influence of coil mean diameter D_0 on the ECT signals is shown in Fig. 6. It can be seen that with increasing D_0, the amplitude of the impedance change increases, which means that the sensitivity increases. Fuel claddings are bundled together with a 0.30~0.45-cm space left between each rod for coolant to flow. Thus, to reduce the influence of the adjacent fuel rod, D_0 should be within 1/2 the diameter of the fuel rod.

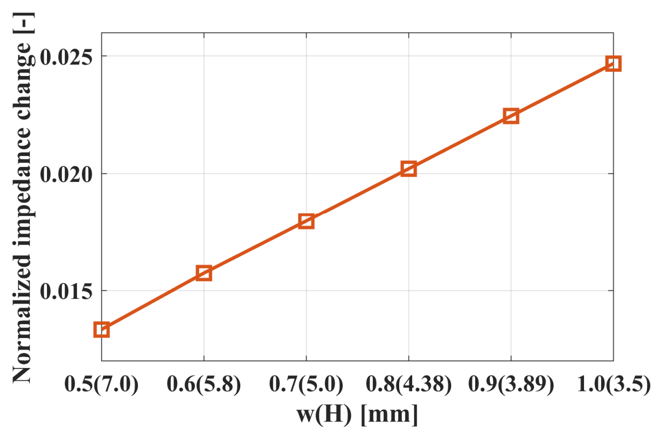

Fig. 6. Influence of coil width/height on ECT signal (f = 300 kHz, D_0 = 3.0 mm, Cr layer = 5 μm, oxide layer = 20 μm).

D. Influence of Coil Width/Height

The influence of the coil w/H on the ECT signals is shown in Fig. 7. It can be seen that under the fixed coil section area, with increasing coil width or decreasing coil height, the amplitude of the impedance change increases, which means that the sensitivity increases. A fat and short coil is thus better than a thin and tall coil.

From the above analysis, the influence of exciting frequency, coil mean diameter, coil width, and coil height on the performance of the ECT probe was analyzed. The performance of the probe can thus be improved as follows:

1. Frequency: In the case of Cr layer detection, the maximum intended thickness should be smaller than twice the skin depth. It insures proper linearity. Within this limitation, the higher the frequency, the higher the sensitivity. In the case of oxide layer detection, the higher the frequency, the higher the sensitivity. However, considering the stray capacitance in the coil, the exciting frequency should be below 10 MHz.
2. Coil mean diameter: The larger the mean diameter, the higher the sensitivity.
3. Coil width/height: The larger the coil width and smaller the coil height, the higher the sensitivity.

IV. Design flowchart for ECT Probe

In this section, the design of the ECT probe was discussed. The parameters of the coil in fabrication are shown in Fig. 7. As an ECT probe belongs to inductive sensors, the designing target maximizes its inductance. The conclusions in Section III provide intuitive guidance for designing the ECT probe. However, the simulation did not consider the resonance and energy efficiency in the inductive sensor. Thus, to actually design an ECT probe for nuclear fuel claddings, we not only added the consideration of avoiding resonance and improving quality factor Q of the probe, but also the consideration of geometry relationship between probe and claddings. In detail, to maintain detection stability, the resonance frequency f_r of the coil should be three times higher than the exciting frequency.

The equation of f_r is expressed by Equation (22). In addition, to reduce the influence of the adjacent cladding, the mean diameter D_0 should be less than 1/2 the diameter of cladding. Using wire diameter d_0, D_0 and f_r, the height H, turn N, and initial weight w_0 can be obtained using Equations (16), (17), and (18). Furthermore, resistance R, capacitance C, and inductance L can be calculated through Equation (19)–(21) [34–36]. Aiming for the maximum L, the H, N, w_0 should be modified according to Section III and the proper Q factor in Equation (23).

$$w = N_L \cdot d_0 \tag{16}$$

$$H = N_V \cdot d_0 \tag{17}$$

$$N = N_L \cdot N_V \tag{18}$$

Finally, a one-directional design flowchart was built, as shown in Fig. 8. A step-by-step explanation of the flowchart is provided below:

Step 1: Determine the exciting frequency according to the intended thickness. In the case of Cr layer detection, the maximum intended thickness should be smaller than twice the skin depth. In the case of oxide layer detection, the higher the frequency, the higher the sensitivity. However, considering the stray capacitance in the coil, the exciting frequency should be below 10 MHz.

Step 2: To ensure the stability of the measurement, set the resonance frequency f_r of the coil to three times the exciting frequency. This can avoid the resonance of coil.

Step 3: To reduce the influence of the adjacent fuel rod, D_0 should be less than 1/2 the diameter of the cladding.

Step 4: According to manufacturing ability, the wire diameter should be decided first; for example, $d_0 = 0.18$ mm. An initial coil width w_0 should be set around 0.5~1.0 mm. Then, according to (16), N_L and R_i are obtained. Using (22), N_v, H, and the initial total coil turn N_0 is obtained based on the resonance frequency f_r. Obtain R, L, and C using (19), (20), and (21).

Step 5: N_v and H should be slowly decreased, while N_L and w should be increased, aiming to obtain the maximum L.

Step 6: In the case of constant resonant frequency, the final N_v and N_L are adjusted to obtain a high Q using (23).

The principle of the proposed design flowchart maximizes inductance within the constraints of resonance frequency and quality factor. In addition, the flowchart gives formulas to calculate coil electrical parameters. The analytical model in Section III can also be used to obtain the inductance of coil in free space. However, it is too difficult for engineers to understand and use without the knowledge of the analytical model. Thus, these approximation formulas are provided to easily and quickly obtain R, C, L, and f_r for practical usage, and the flowchart is intuitively reasonable and easy to use. The experimental validation of the equations and flowchart are shown in Section V.

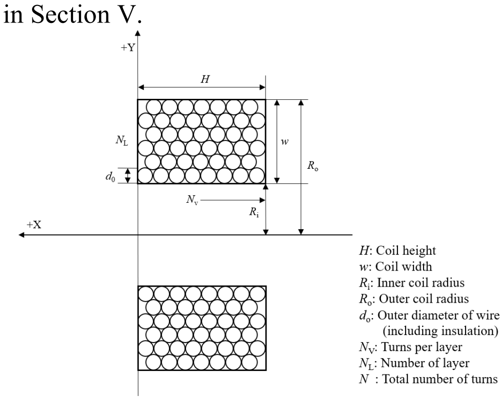

Fig. 7. Coil parameters.

This article has been accepted for publication in IEEE Transactions on Instrumentation and Measurement. This is the author's version which has not been fully edited and content may change prior to final publication. Citation information: DOI 10.1109/TIM.2025.3545170

$$R = \frac{2\rho_c}{d_0} N\left(2R_\mathrm{i} + (2N_\mathrm{L} - 1)\right)[\Omega] \tag{19}$$

$$\begin{aligned} L &= \mu_\mathrm{r}(N_\mathrm{V}N_\mathrm{L})^2(2R_\mathrm{i} + N_\mathrm{L}d_0) \\ &= \left[k - \frac{2\pi N_\mathrm{L}}{N_\mathrm{V}}\left(\left(0.693 + 0.32\left(1 - e^{\frac{-N_\mathrm{V}}{4.2N_\mathrm{L}}}\right)\right)\right)\right] \\ &\times 10^{-10}\ [\mathrm{H}] \end{aligned} \tag{20}$$

$$C = \frac{8\pi\varepsilon_0\varepsilon_\mathrm{r}N_\mathrm{V}d_0(N_\mathrm{L} - 1)}{6\tilde{d}N_\mathrm{L}^2}(2R_\mathrm{i} + d_0)\ [\mathrm{pF}] \tag{21}$$

$$f_\mathrm{r} = \frac{1}{2\pi\sqrt{LC}} = \frac{1}{2\pi\sqrt{\frac{8\pi\varepsilon_0\varepsilon_\mathrm{r}N_\mathrm{V}^3d_0(2R_\mathrm{i}+d_0)(2R_\mathrm{i}+N_\mathrm{L}d_0)(N_\mathrm{L}-1)\left[k - \frac{2\pi N_\mathrm{L}}{N_\mathrm{V}}\left(0.693 + 0.32\left(1 - e^{\wedge}\left(\frac{-N_\mathrm{V}}{4.2N_\mathrm{L}}\right)\right)\right)\right] \times 10^{-10}}{6\tilde{d}}}} \tag{22}$$

$$Q = \frac{2\pi f L}{R} \tag{23}$$

ρ_c, resistivity of wire, $1.65\times10^{-5}(\Omega\cdot\mathrm{mm}^2/\mathrm{mm})$;
μ_r, relative permeability of coil core;
$k = a\ln(D_0/H) + b(D_0/H) + c$, a, b, and c are determined in Table IV; D_0 is the mean diameter of the coil, H is the height of the coil;
ε_0, vacuum permittivity, 8.854×10^{-3}(pF/mm); ε_r, relative permittivity, 2.1;
$\tilde{d}$, distance between layers, $\tilde{d} = 1.26d_0 - 1.15d_\mathrm{i}$; d_i, inner diameter of wire, d_i = 0.399 mm. d_0, diameter of wire.

TABLE IV
DETERMINATION OF PARAMETERS *a*, *b*, AND *c*

D_0/H	a	b	c
<1	1.2317	3.7450	3.0500
1~4.5	4.6630	0.3803	6.4147
4.5~100	6.1350	0.0070	5.7100

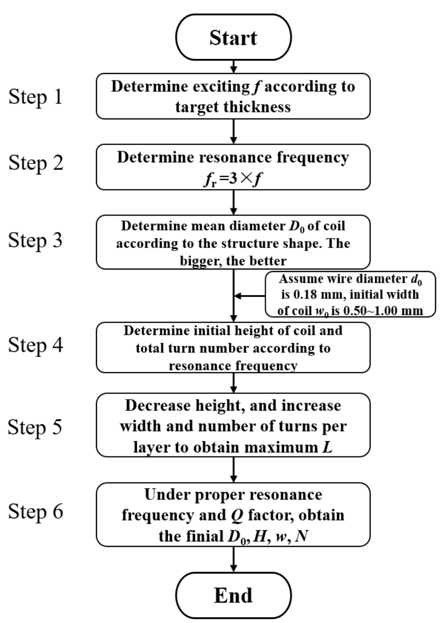

Fig. 8. Flowchart of the coil design.

V. MODEL VALIDATION AND TEST OF THE NEW PROBE

In this section, the model proposed in Section II is validated and compared with the FEM model. Moreover, the equations in Section IV are tested. Finally, the new probe designed by the proposed flowchart is compared with the old one.

A. Experimental Device

The arrangement of the experimental devices is shown in Fig. 9. A cladding was fixed on a table by a fixture. The ECT probe was fixed with a jig, and a micrometer in the jig was used to control the distance between the bottom of the ECT probe and the surface of cladding, which was also called the liftoff distance. The impedance of the coil was measured using a commercial LCR meter VICTOR 4092C. The sensitivity of the meter is 0.001 pF and 0.001 mΩ. The accuracy is 0.05%.

According to the design flowchart in Section IV, a new ECT probe was designed. To reduce the costs of the design, old and new probes were constructed with the same inner diameters. The exciting frequency was 200 kHz. The turns of the two probes were 120. The parameters of the two probes are shown in Table V.

Used cladding containing a Zr pipe, Cr layer, and oxide layer is radioactive. Thus, in the experiment, a new cladding containing Zr pipe and Cr layer was detected. Since there was no oxide layer present, and because the oxide layer is a nonconductive and nonferromagnetic substance, the liftoff distance between the bottom of the probe and the top of the Cr layer was used to simulate the oxide layer in a three-layer cladding measurement. The micrometer was employed to precisely control the distance. Moreover, it was assumed that the probe was in direct contact with the simulated oxide layer.

The diameter of the Zr pipe was 8.36 mm. The thickness of the Cr layer was 10 µm. The conductivity and permeability of Zr and Cr are the same as those in the simulation, as shown in Table I.

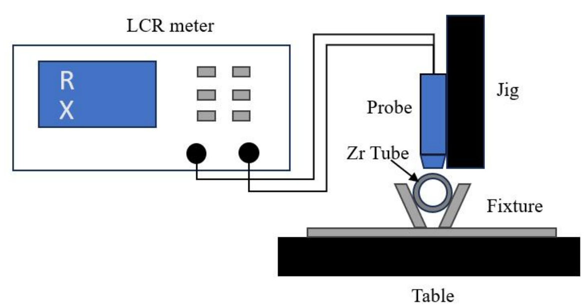

Fig. 9. Experimental devices.

TABLE V
PARAMETERS OF OLD AND NEW ECT PROBES

	Mean diameter [mm]		Width [mm]		Height [mm]	
	Design Value	Measured Value	Design Value	Measured Value	Design Value	Measured Value
Old probe	3.50	3.57	0.50	0.62	7.00	7.05
New probe	4.50	4.36	1.50	1.44	3.00	2.95

B. Results and Discussion

Using the equations detailed in Section IV, the electrical parameters of the old coil are calculated and shown in Table VI. The LCR meter was used to measure the actual parameters. The measured values are also shown in Table VI. The measured values with the calculated values. The maximum error of 20% may be due to the manufacturing discrepancy shown in Table V.

This article has been accepted for publication in IEEE Transactions on Instrumentation and Measurement. This is the author's version which has not been fully edited and content may change prior to final publication. Citation information: DOI 10.1109/TIM.2025.3545170

TABLE VI
COMPARISON OF MEASURED AND CALCULATED VALUES

	Resistance R [Ω]	Inductance L [uH]	Capacitance C [pF]
Calculation	0.81	17.05	17.39
Measurement	1.03	19.06	22.60

To validate the analytical model proposed in Section II, old and new probes were calibrated in advance using the method in [37]. In this method, both coil liftoff and sample conductivities were first measured and then fitted. The coil dimension uncertainties were reduced. Cladding was detected by two probes through experimental and simulation methods. To improve the stability of the experimental results, the measurements were taken 10 times, and the average value was compared with the simulation result. To further prove the superiority of the analytical model to the FEM model, commercial software COMSOL was used to carry out FEM analysis. The element numbers in the old and new probe models were 251868 and 259305, respectively.

When evaluating Eq. (15), the semi-infinite integration with respect to α and semi-infinite summation with respect to m should be truncated to suitable numbers α_{max} and m_{max} respectively. In this paper, taking into account the calculation time and accuracy, we set the step size, α_{max} and m_{max} as 25, 2500, and 6, respectively.

A comparison of the results is shown in Fig. 10. Under the two probes, the simulation results match the experimental results well. The comparison verifies the proposed analytical model. The computer used in the simulation had an AMD Ryzen7 6800H CPU and 16 GB memory. The computing time of FEM was around 7 minutes. In contrast, the computing time of the analytical model was around 17 seconds. Comparing to the experimental results, the average error of FEM model was 4.1%. In contrast, the average error of analytical model was 1.8%. The comparison validated the merit of the analytical model.

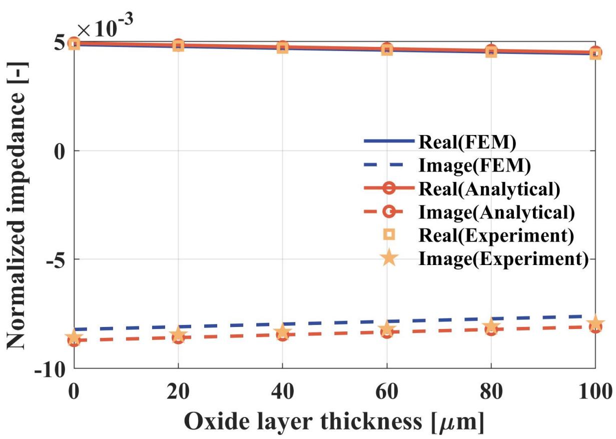

(a) Old probe

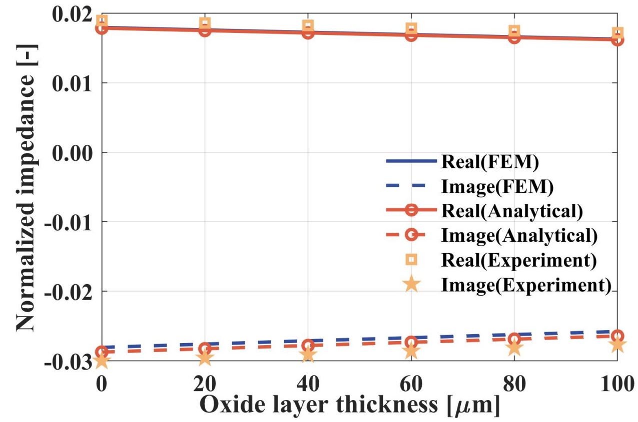

(b) New probe

Fig. 10. Comparison of experimental and simulation results.

Finally, the performances of the old and new probes were compared through experiment, and the results are shown in Fig. 11. The comparison shows that the signal amplitude of the new probe was greater than that of the old probe. Moreover, the sensitivity of the old and new coils was 7.75 /um, 29.09 /um. This means that the sensitivity of the new probe was larger than that of the old probe. These results indicate that the proposed probe design flowchart in this paper is effective.

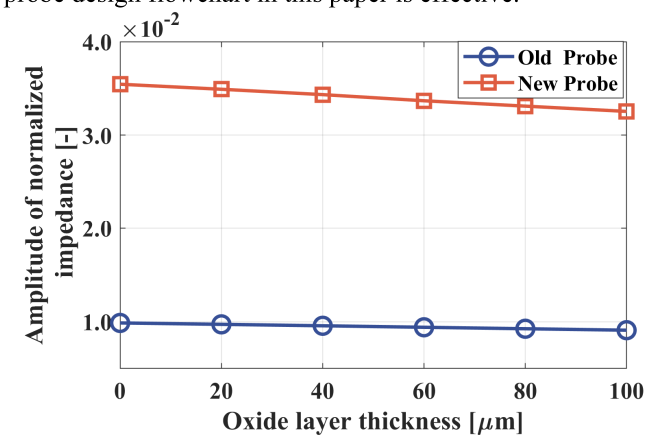

Fig. 11. Performance comparison of old and new probes.

VI. CONCLUSION

The design and optimization of an ECT pancake probe for the thickness measurement of multilayers in fuel claddings was studied in this paper. SOVP was used to build the analytical model for a pancake probe above a multilayer pipe with arbitrary nonconductive and conductive layers. The analytical model was validated and efficient compared with the FEM model. Moreover, the model was used to study the influence of the exciting frequency and coil parameters on the sensitivity of the ECT probe. The analysis indicates that the larger the mean diameter of the coil, the higher the sensitivity. However, fuel claddings are bundled together, with 0.30~0.45 cm of space left between each cladding for the coolant to flow. Thus, to reduce the influence of the adjacent cladding, D_0 should be less than 1/2 the diameter of the cladding. Therefore, fat and short coil is better than a thin and tall coil.

A design flowchart for the probe that further considers resonance frequency and the quality factor was proposed. A new probe was developed based on the proposed design flowchart, and a testing experiment was carried out. The performance of the newly designed probe was better and more

This article has been accepted for publication in IEEE Transactions on Instrumentation and Measurement. This is the author's version which has not been fully edited and content may change prior to final publication. Citation information: DOI 10.1109/TIM.2025.3545170

sensitive than that of the old probe.

In this paper, an analytical model of ECT problem including three layers was proposed. However, when the layer number of pipe was changed, the whole equations need to be solved. Thus, the proposed model was not convenient for the multilayer with arbitrary layer number. In the future, Cheng matrix method will be added to improve the convenience of model.

Appendix

Given the two adjacent conductive layers and one nonconductive layer above, a system of ten linear equations is constructed as an example as follows:

$$\left(\frac{\partial^2 W_{a2}}{\partial\rho\partial z}-\frac{\partial^2 W_{a1}}{\partial\rho\partial z}-\frac{k_1^2\partial W_{b2}}{\rho\partial\varphi}\right)|_{\rho=r_1}=0 \tag{A1}$$

$$\left(\frac{1}{\rho}\frac{\partial^2 W_{a2}}{\partial\varphi\partial z}-\frac{\mu_{r1}}{\rho}\frac{\partial^2 W_{a1}}{\partial\varphi\partial z}+\frac{k_1^2\partial W_{b2}}{\partial\rho}\right)|_{\rho=r_1}=0 \tag{A2}$$

$$\left(\frac{\partial^2 W_{a2}}{\partial z^2}-\mu_{r1}\frac{\partial^2 W_{a1}}{\partial z^2}+k_1^2 W_{a2}\right)|_{\rho=r_1}=0 \tag{A3}$$

$$\left(\frac{\partial^2 W_{a3}}{\partial\rho\partial z}-\frac{k_2^2\partial W_{b3}}{\rho\partial\varphi}-\left(\frac{\partial^2 W_{a2}}{\partial\rho\partial z}-\frac{k_1^2\partial W_{b2}}{\rho\partial\varphi}\right)\right)|_{\rho=r_2}=0 \tag{A4}$$

$$\left(\left(\frac{1}{\rho}\frac{\partial^2 W_{a3}}{\partial\varphi\partial z}+\frac{k_2^2\partial W_{b3}}{\partial\rho}\right)\mu_{r1}-\left(\frac{1}{\rho}\frac{\partial^2 W_{a2}}{\partial\varphi\partial z}+\frac{k_1^2\partial W_{b2}}{\partial\rho}\right)\mu_{r2}\right)|_{\rho=r_2}=0 \tag{A5}$$

$$\left(\left(\frac{\partial^2 W_{a3}}{\partial z^2}+k_2^2 W_{a3}\right)\mu_{r1}-\left(\frac{\partial^2 W_{a2}}{\partial z^2}+k_1^2 W_{a2}\right)\mu_{r2}\right)|_{\rho=r_2}=0 \tag{A6}$$

$$\left(\frac{\partial^2 W_{a3}}{\partial\rho\partial z}-\frac{\partial^2 W_{a4}}{\partial\rho\partial z}-\frac{k_2^2\partial W_{b3}}{\rho\partial\varphi}\right)|_{\rho=r_3}=0 \tag{A7}$$

$$\left(\frac{1}{\rho}\frac{\partial^2 W_{a3}}{\partial\varphi\partial z}-\frac{\mu_{r2}}{\rho}\frac{\partial^2 W_{a4}}{\partial\varphi\partial z}+\frac{k_2^2\partial W_{b3}}{\partial\rho}\right)|_{\rho=r_3}=0 \tag{A8}$$

$$\left(\frac{\partial^2 W_{a3}}{\partial z^2}-\mu_{r2}\frac{\partial^2 W_{a4}}{\partial z^2}+k_2^2 W_{a3}\right)|_{\rho=r_3}=0 \tag{A9}$$

$$\left(\frac{1}{\rho}\frac{\partial W_{a3}}{\partial\varphi}-\frac{\partial W_{b3}}{\partial\rho\partial z}-\left(\frac{1}{\rho}\frac{\partial W_{a2}}{\partial\varphi}-\frac{\partial W_{b2}}{\partial\rho\partial z}\right)\right)|_{\rho=r_2}=0 \tag{A10}$$

By substituting (7)–(12) into (A1)–(A10) and using the orthogonality of the exponential functions, the relationships between the unknown coefficients C_1, C_{a2}, D_{a2}, C_{b2}, D_{b2}, C_{a3}, D_{a3}, C_{b3}, and D_{ec} and coil coefficient C_s are achieved as:

$$\begin{bmatrix}
\alpha r_1|\alpha|\mathrm{I}'_{m1} & -\alpha r_1\alpha_{k1}\mathrm{I}'_{m3} & -\alpha r_1\alpha_{k1}\mathrm{K}'_{m3} & mk_1^2\mathrm{I}_{m3} & mk_1^2\mathrm{K}_{m3} & 0 & 0 & 0 & 0 & 0\\
\alpha m\mu_{r1}\mathrm{I}_{m1} & -\alpha m\mathrm{I}_{m3} & -\alpha m\mathrm{K}_{m3} & k_1^2 r_1\alpha_{k1}\mathrm{I}'_{m3} & k_1^2 r_1\alpha_{k1}\mathrm{K}'_{m3} & 0 & 0 & 0 & 0 & 0\\
-\alpha^2\mu_{r1}\mathrm{I}_{m1} & \alpha_{k1}^2\mathrm{I}_{m3} & \alpha_{k1}^2\mathrm{K}_{m3} & 0 & 0 & 0 & 0 & 0 & 0 & 0\\
0 & -\alpha r_2\alpha_{k1}\mathrm{I}'_{m4} & -\alpha r_2\alpha_{k1}\mathrm{K}'_{m4} & mk_1^2\mathrm{I}_{m4} & mk_1^2\mathrm{K}_{m4} & \alpha r_2\alpha_{k2}\mathrm{I}'_{m5} & \alpha r_2\alpha_{k2}\mathrm{K}'_{m5} & -mk_2^2\mathrm{I}_{m5} & -mk_2^2\mathrm{K}_{m5} & 0\\
0 & \alpha m\mu_{r2}\mathrm{I}_{m4} & \alpha m\mu_{r2}\mathrm{K}_{m4} & -k_1^2\mu_{r2}r_2\alpha_{k1}\mathrm{I}'_{m4} & -k_1^2\mu_{r2}r_2\alpha_{k1}\mathrm{K}'_{m4} & -\alpha m\mu_{r1}\mathrm{I}_{m5} & -\alpha m\mu_{r1}\mathrm{K}_{m5} & k_2^2\mu_{r1}r_2\alpha_{k2}\mathrm{I}'_{m5} & k_2^2\mu_{r1}r_2\alpha_{k2}\mathrm{K}'_{m5} & 0\\
0 & -\alpha_{k1}^2\mu_{r2}\mathrm{I}_{m4} & -\alpha_{k1}^2\mu_{r2}\mathrm{K}_{m4} & 0 & 0 & \alpha_{k2}^2\mu_{r1}\mathrm{I}_{m5} & \alpha_{k2}^2\mu_{r1}\mathrm{K}_{m5} & 0 & 0 & 0\\
0 & 0 & 0 & 0 & 0 & -\alpha r_3\alpha_{k2}\mathrm{I}'_{m6} & -\alpha r_3\alpha_{k2}\mathrm{K}'_{m6} & mk_2^2\mathrm{I}_{m6} & mk_2^2\mathrm{K}_{m6} & \alpha r_3|\alpha|\mathrm{K}'_{m2}\\
0 & 0 & 0 & 0 & 0 & -\alpha m\mathrm{I}_{m6} & -\alpha m\mathrm{K}_{m6} & k_2^2 r_3\alpha_{k2}\mathrm{I}'_{m6} & k_2^2 r_3\alpha_{k2}\mathrm{K}'_{m6} & \alpha m\mu_{r2}\mathrm{K}_{m2}\\
0 & 0 & 0 & 0 & 0 & \alpha_{k2}^2\mathrm{I}_{m6} & \alpha_{k2}^2\mathrm{K}_{m6} & 0 & 0 & -\alpha^2\mu_{r2}\mathrm{K}_{m2}\\
0 & -m\mathrm{I}_{m4} & -m\mathrm{K}_{m4} & \alpha r_2\alpha_{k1}\mathrm{I}'_{m4} & \alpha r_2\alpha_{k1}\mathrm{K}'_{m4} & m\mathrm{I}_{m5} & m\mathrm{K}_{m5} & -\alpha r_2\alpha_{k2}\mathrm{I}'_{m5} & -\alpha r_2\alpha_{k2}\mathrm{K}'_{m5} & 0
\end{bmatrix}
\cdot
\begin{bmatrix} C_1\\ C_{a2}\\ D_{a2}\\ C_{b2}\\ D_{b2}\\ C_{a3}\\ D_{a3}\\ C_{b3}\\ D_{b3}\\ D_{ec}\end{bmatrix}
=
\begin{bmatrix} 0\\ 0\\ 0\\ 0\\ 0\\ 0\\ -\alpha r_3|\alpha|\mathrm{I}'_{m2}C_s\\ -\alpha m\mu_{r2}\mathrm{I}_{m2}C_s\\ \alpha^2\mu_{r2}\mathrm{I}_{m2}C_s\\ 0\end{bmatrix} \tag{A11}$$

The first-order Bessel functions are uniformly abbreviated into symbolic form as follows:

$\mathrm{I}_{m1}=\mathrm{I}_m(|\alpha|r_1)$, $\mathrm{I}_{m2}=\mathrm{I}_m(|\alpha|r_3)$, $\mathrm{I}_{m3}=\mathrm{I}_m(\alpha_{k1}r_1)$, $\mathrm{I}_{m4}=\mathrm{I}_m(\alpha_{k1}r_2)$, $\mathrm{I}_{m5}=\mathrm{I}_m(\alpha_{k2}r_2)$, $\mathrm{I}_{m6}=\mathrm{I}_m(\alpha_{k2}r_3)$, $\mathrm{K}_{m1}=\mathrm{K}_m(|\alpha|r_1)$, $\mathrm{K}_{m2}=\mathrm{K}_m(|\alpha|r_3)$, $\mathrm{K}_{m3}=\mathrm{K}_m(\alpha_{k1}r_1)$, $\mathrm{K}_{m4}=\mathrm{K}_m(\alpha_{k1}r_2)$, $\mathrm{I}_{m5}=\mathrm{K}_m(\alpha_{k2}r_2)$, $\mathrm{I}_{m6}=\mathrm{K}_m(\alpha_{k2}r_3)$.

Then, the unknown coefficient C_1, C_{a2}, D_{a2}, C_{b2}, D_{b2}, C_{a3}, D_{a3}, C_{b3}, D_{b3}, and D_{ec} can be obtained by solving the matrix (A11).

References

[1] A. T. Motta, A. Couet, and R. J. Comstock, "Corrosion of zirconium alloys used for nuclear fuel cladding," *Annu. Rev. Mater. Sci.*, vol. 45, no. 1, pp. 311–343, 2015.

[2] L. A. Karpyuk *et al.*, "Accident tolerant fuel with chromium-coated fuel-rod cladding," *At. Energy*, vol. 130, no. 3, pp. 149–155, 2021.

[3] G. Cosarinsky *et al.*, "Automatic eddy current classification of signals delivered by flaws–Application to nuclear fuel cladding," *INSIGHT*, vol. 54, no. 6, pp. 316–321, 2012.

[4] J. García–Martín, J. Gómez–Gil, and E. Vázquez-Sánchez, "Non–destructive techniques based on eddy current testing," *Sensors*, vol. 11, no. 3, pp. 2525–2565, 2011.

[5] N. Zhang *et al.*, "Eddy current probe with three-phase excitation and integrated array tunnel magnetoresistance sensors," *IEEE Trans. Ind. Electron.*, vol. 68, no. 6, pp. 5325–5336, 2020.

[6] R. Montgomery *et al.*, "Sister rod nondestructive examination final report," Oak Ridge National Lab, Oak Ridge, TN, USA, 2018.

[7] W. Li *et al.*, "A thickness measurement system for metal films based on eddy-current method with phase detection," *IEEE Trans. Ind. Electron.*, vol. 64, no. 5, pp. 3940–3949, 2017.

[8] J. W. Park *et al.*, "Thickness evaluation of Cr coating fuel rod using encircling ECT sensor," *Nucl. Eng. Technol.*, vol. 54, no. 9, pp. 3272–3282, 2022.

[9] J. W. Park *et al.*, "Thickness measurements of a Cr coating deposited on Zr–Nb alloy plates using an ECT pancake sensor," *Nucl. Eng. Technol.*, vol. 55, no. 9, pp. 3260–3267, 2023.

[10] A. S. Krukov *et al.*, "Design of multiprobe for fuel-elements cladding eddy current testing," *Am J Phys.*, vol. 1636, no. 1, p. 12014, 2020.

[11] T. J. Rocha *et al.*, "Studies to optimize the probe response for velocity induced eddy current testing in aluminium," *Measurement*, vol. 67, pp. 108–115, 2015.

[12] S. She *et al.*, "Optimal design of remote field eddy current testing probe for ferromagnetic pipeline inspection," *Measurement*, vol. 168, p. 108306, 2021.

[13] K. N. Azaman, A. Sophian, and F. Nafiah, "Effects of Coil Diameter in Thickness Measurement Using Pulsed Eddy Current Non-Destructive Testing", *MSE.*, IOP Publishing, vol. 260, no. 1, p. 012001, 2017.

[14] L. S. Rosado *et al.*, "Geometric optimization of a differential planar eddy currents probe for non–destructive testing," *Sens. Actuator A Phys.*, vol. 197, pp. 96–105, 2013.

[15] B. A. Auld, F. G. Muennemann, and G. L. Burkhardt, "Experimental methods for eddy current probe design and testing," *Rev. prog. quant. nondestruct. eval*, vol. 3A, pp. 477–488, 1984.

[16] H. R. Parsa, S. A. Gholamian, and M. Abbasi, "Design and optimization of eddy current testing probe using bees algorithm and finite element analysis," *IJMECS*, vol. 5 no. 12, pp. 40–46, 2013.

[17] D. I. Ona *et al.*, "Design and optimisation of mutual inductance based pulsed eddy current probe," *Measurement*, vol. 144, pp. 402–409, 2019.

[18] L. S. Rosado *et al.*, "A differential planar eddy currents probe: Fundamentals, modeling and experimental evaluation," *NDT&E Int.*, vol. 51, pp. 85–93, 2012.

[19] A. N. AbdAlla *et al.*, "Challenges in improving the performance of eddy current testing," *Meas. Control.*, vol. 52, no. 1–2, pp. 46–64, 2019.

[20] N. O. Romero–Arismendi *et al.*, "Design method for a GMR–based eddy current sensor with optimal sensitivity," *Sens. Actuator A Phys.*, vol. 314, p. 112348, 2020.

[21] B. Delabre, J. Decitre, and Y. Le Bihan, "Design of a flexible eddy current probe in view of the evaluation of the electrical conductivity during inspection of defects," *Nondestruct. Test. Evaluation*, vol. 32, no. 3, pp. 227–241, 2017.

[22] M. Kako *et al.*, "Probe design for the eddy current inspection of cooling tubes in the blanket of a fusion DEMO reactor," *Plasma Fusion Res*, vol. 17, pp. 2405102–2405102, 2022.

[23] D. Zhou, G. Y. Tian, and Y. Li, "Simulation based on optimisation of pulsed eddy current probe design," *Nondestruct. Test. Eva.*, vol. 25, no. 3, pp. 219–230, 2010.

[24] T. Theodoulidis. "Developments in efficiently modelling eddy current testing of narrow cracks," *NDT&E Int.*, vol. 43, no.7, pp.591–598, 2010.

[25] M. Fan *et al.*, "Analytical modeling for transient probe response in pulsed eddy current testing". *NDT&E Int.*, vol. 42, no.5, pp. 376–383, 2009.

[26] C. Li *et al.*, "Accurate thickness measurement using eddy current system based on novel transformer model." *IEEE T. Instrum. Meas.*, vol. 71, pp.1–12, 2022.

[27] C. V. Dodd and W. E. Deeds, "Analytical solutions to eddy–current probe–coil problems," *J. Appl. Phys*, vol. 39, no. 6, pp. 2829–2838, 1968.

[28] C. V. Dodd, C. C. Cheng, and W. E. Deeds, "Induction coils coaxial with an arbitrary number of cylindrical conductors," *J. Appl. Phys*, vol. 45, no. 2, pp. 638–647, 1974.

[29] N. M. Sakaji, "Force and eddy currents in a solid conducting cylinder due to an eccentric circular current loop," *J. Phys. D.*, vol. 33, no. 18, pp. 2239–2248, 2000.

[30] T. Theodoulidis and A. Skarlatos, "Eddy current interaction of an arbitrarily positioned probe coil with a conductive cylinder," *IEEE Trans. Magn.*, vol. 48, no. 8, pp. 2392–2394, 2012.

[31] X. Mao and Y. Lei, "Analytical solutions to eddy current field excited by a probe coil near a conductive pipe," *NDT&E Int.*, vol. 54, pp. 69–74, 2013.

[32] B. Wan, B. Hu, and X. Chen. "Analytical solutions for flexible circular spiral eddy current array coils inside a conductive tube under different operation modes." *NDT&E Int.*, no. 131, pp. 102693, 2022.

[33] B. Wan and X. Chen, "Gap Measurement of Double-Layer Metal Tube Based on Analytical Solution of Eddy Current Array Under Transmit–Receive Mode," *IEEE T Instrum Meas*, vol. 72, pp. 1–10, 2023.

[34] J. Martínez, B. Slobodan, and A. Cevdet. "On evaluation of inductance, DC resistance, and capacitance of coaxial inductors at low frequencies." *IEEE Trans. Magn.*, vol. 50, no.7, pp. 1–12, 2014.

[35] X. Zhao, "Practical Power Technical Handbook Magnetic Components Fascicle", ShengYang: LiaoNing Science and Technology Publishing House, pp. 32 – 40, 2002.

[36] J. Gao and F. Wang, "Correction and Interference of the Distributed Capacitance of Inductor Coil on Electrical Measurement," Colliery Mechanical & Electrical Technology, vol. 6, pp. 46–47, 2010.

[37] D. J. Harrison, L. D. Jones, and S. K. Burke, "Benchmark problems for defect size and shape determination in eddy-current nondestructive evaluation," *J. Nondestr. Eval.*, vol. 15, pp. 21–34, 1996.

Jiuhao Ge received the Ph.D. degree in mechanical and electronics engineering from the China University of Petroleum, China, in 2018. Following graduation, he joined the Nanjing University of Aeronautics and Astronautics, where he is currently an associate professor of Measurement Science and Engineering.

From 2019 to 2021, he was a research fellow with the Japan Society for the Promotion of Science, Japan. His research interest includes electromagnetic nondestructive testing technique and inversion problem.

Fei Xu graduated from Nanchang Hangkong University in Jiangxi Province in 2022 with a bachelor's degree. He is currently pursuing a master's degree in instrument science and technology at the School of Automation, Nanjing University of Aeronautics and Astronautics.

His current research interests are eddy current semi-analytical modeling and electromagnetic nondestructive testing of zirconium tubes in nuclear power plants.

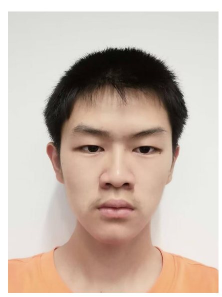

Jia Chen graduated from Nanjing University of Aeronautics and Astronautics in China in 2023 with a bachelor's degree. He is currently studying for a master's degree in instrument science and technology at the School of Automation, Nanjing University of Aeronautics and Astronautics.

His current research direction is electromagnetic nondestructive testing

Weiyu Jiang graduated from China University of Petroleum with a master's degree in 2020. He currently works at Nuclear Power Institute of China.

His current research interests are electromagnetic nondestructive testing for poolside inspection of nuclear power plants.

Zhiyong Deng received his Master of Science degree in Nuclear Technology and Application from the Department of Engineering Physics of Tsinghua University in 2011. He currently works at Nuclear Power Institute of China.

His current research interests are nondestructive testing of nuclear